SIMULATION STUDY OF TISSUE TYPE DIFFERENTIATION USING NON-NEGATIVE MATRIX FACTORIZATION

Yuqian Li[1,2,3], Diana M. Sima[2,3], Sofie Van Cauter[4,5], Uwe Himmelreich[5], Yiming Pi[1], Sabine Van Huffel[2,3]

[1]*School of Electronic Engineering, University of Electronic Science and Technology of China, Xiyuan Dadao 2006, Chengdu, China*

[2]*Department of Electrical Engineering, ESAT-SCD, Katholieke Universiteit Leuven, Leuven, Belgium*

[3] *IBBT-K.U.Leuven Future Health Department, Leuven, Belgium*

[4] *Department of Radiology, University Hospitals of Leuven, Leuven, Belgium.*

[5]*Biomedical NMR Unit/Molecular Small Animal Imaging Center, Department of Medical Diagnostic Sciences, Katholieke Universiteit Leuven, Leuven, Belgium*

{Yuqian.Li, Diana.Sima, Sabine.VanHuffel}@esat.kuleuven.be, sofie.vancauter@uz.kuleuven.ac.be, Uwe.Himmelreich@med.kuleuven.be, ympi@uestc.edu.cn

Keywords: Glioma: Magnetic Resonance Spectroscopic Imaging (MRSI): Non-negative Matrix Factorization (NMF): Blind Source Separation (BSS)

Abstract: Finding the brain tumor tissue-specific magnetic resonance spectra and their corresponding spatial distribution is a typical Blind Source Separation (BSS) problem. Non-negative Matrix Factorization (NMF), which only requires non-negativity constraints, has become popular because of its advantages compared to other BSS methods. A variety of algorithms based on traditional NMF have been recently proposed. This study focuses on the performance comparison of several NMF implementations, including some newly released methods, in brain glioma tissue differentiation using simulated magnetic resonance spectroscopic imaging (MRSI) signals. Experimental results demonstrate the possibility of finding typical tissue types and their distributions using NMF algorithms. The (accelerated) hierarchical alternating least squares algorithm was found to be the most accurate.

1 INTRODUCTION

Automatic tissue type differentiation in brain tumor patients is of utmost importance in guiding therapy and determining prognosis. Magnetic resonance spectroscopic imaging (MRSI) (Brown et al., 1982), which produces localized spectra, is used as a non-invasive tool for additional clinical diagnosis of brain tumors; see Figure 1. Given an $m \times n$ matrix X which represents the observed spectra from MRSI data, each column containing a spectrum from one voxel, previous studies (Su et al., 2008) demonstrated that X can be approximately described as a linear combination of constituent specta of different tissue types. The model is

$$X = WH + N \quad (1)$$

W is a $m \times r$ matrix, with each column representing a recovered spectrum for each tissue type. Each row of the $r \times n$ matrix H contains the linear combination weights (interpreted here as abundances or concentrations) of all constituent tissue spectra. N stands for additive measurement noise.

Blind Source Separation (BSS) is one of the main approaches to perform such factorization. One

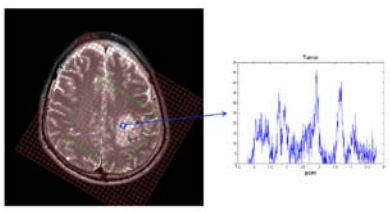


Figure 1: Left: anatomic image of a glioma patient's brain overlaid with the MRSI grid. Right: the spectral profile from the blue voxel from the tumor area.

of the algorithms, non-negative matrix factorization (NMF) (Lee et al., 1999), has attracted much attention in recent years because it does not require the constituent spectra to be orthogonal or independent. The mathematical formulation of the basic NMF problem is

$$\min_{W,H} f(W,H) = \frac{1}{2} \| X - WH \|_F^2 \quad \text{subject to} \quad \forall ij, W_{ij}, H_{ij} \geq 0 \tag{2}$$

In this paper, we designed a simulation study aiming to evaluate the accuracy of several popular NMF implementations in solving the brain glioma tissue type differentiation problem. The algorithms' performance was investigated specifically in terms of their accuracy to estimate tissue-specific spectra and their spatial distribution.

2 NMF ALGORITHMS

In this section we describe several NMF algorithms that will be compared in Section 4.

- **Multiplicative update method using Euclidean distance measure (mu)** (Lee et al., 2001)**:**
  This algorithm is used most commonly in solving the NMF problem. It uses the Euclidean distance as a measure to construct the cost function $\| X - WH \|^2$. The cost function is minimized using the update rule:

$$H_{kj} \leftarrow H_{kj} \frac{(W^T X)_{kj}}{(W^T WH)_{kj}}$$
$$W_{ik} \leftarrow W_{ik} \frac{(XH^T)_{ik}}{(WHH^T)_{ik}} \tag{3}$$
$$\forall\, i, j, k$$

- **Alternating least squares (als)** (Berry et al., 2007)**:** This algorithm alternately solves unconstrained least squares subproblems for W and H (see Eq. 4) and sets the negative elements to zero.

$$W \leftarrow \arg\min \| X - WH \|_F^2$$
$$H \leftarrow \arg\min \| X - WH \|_F^2 \tag{4}$$

- **Alternating non-negative least squares using projected gradients (cjlin)** (Lin,2007)**:** In this implementation, non-negatively constrained least squares subproblems are solved alternatively for W and H using the projected gradient method. Consider the following standard form of bound-constrained optimization problems:

$$\min_{x \in R^n} f(x) \quad \text{subject to}: l_i \leq x_i \leq u_i, \quad i = 1, \ldots, n \tag{5}$$

Projected gradient methods are iterative and update the current solution x^k to the following x^{k+1} by the rule:

$$x^{k+1} = P[x^k - \alpha^k \nabla f(x^k)] \tag{6}$$

where α^k is the step size and

$$P[x_i] = \begin{cases} x_i & if \quad l_i < x_i < u_i \\ u_i & if \quad x_i \geq u_i \\ l_i & if \quad x \leq l_i \end{cases}$$

Hierarchical alternating least squares (hals) (Cichocki et al., 2007; Cichocki et al., 2009)**: hals** sequentially estimates one column of W and/or one row of H while fixing all the other ones, that is:

$$W_{:k} \leftarrow \arg\min_{W_{:k} \geq 0} \| X - WH \|_F^2 = \arg\min_{W_{:k} \geq 0} \| X - W_{-k} H_{-k} - W_{:k} H_{k:} \|_F^2$$
$$H_{k:} \leftarrow \arg\min_{H_{k:} \geq 0} \| X - WH \|_F^2 = \arg\min_{H_{k:} \geq 0} \| X - W_{-k} H_{-k} - W_{:k} H_{k:} \|_F^2 \tag{7}$$

where $W_{:k}$, W_{-k}, $H_{k:}$, H_{-k} denote, respectively, the kth column of W, the matrix W without the kth column, the kth row of H, and the matrix H without the kth row.

- **Accelerated multiplicative update method (amu) and Accelerated HALS (ahals)** (Gillis, 2011)**:** These two more efficient methods are developed based on the **mu** and **hals** methods. Computational cost is reduced by updating W several times before updating H (and vice versa), instead of updating W and H alternately. An inner loop stopping criterion is utilized for each $W^{(l)}$, defined as the iterate after l updates of W using Eq. 3 for **amu** or Eq. 7 for **ahals** (while H is being kept fixed):

$$\| W^{(l+1)} - W^{(l)} \|_F \leq \delta \| W^{(1)} - W^{(0)} \|_F \quad (8)$$

where δ is a small constant, equal to 0.01 in the implementation.

3 EXPERIMENT & RESULTS

3.1 Simulated spatial distribution

In order to construct a realistic MRSI grid containing spectra from normal tissue, as well as tumor tissue and necrosis, we simulated an MRSI grid in which these 3 tissue types are contained. Table 1 shows the simulated distribution of brain tissues. Each table cell represents a voxel. C, N, and T denote respectively control tissue type (i.e., normal tissue), tumor tissue and necrotic tissue. In the voxels at the interface between tissues, there is usually a mixture of different tissue types. Therefore, decimals are placed into the table to represent concentration of mixed tissues. For instance, 0.8C+0.2T denotes the tissue type in a voxel composed of approximately 80% normal and 20% tumor tissue.

3.2 Simulated MRSI signals

In our study, the simulated signals are linear combinations of 9 metabolite profiles (two simulated lipid profiles and seven metabolite profiles measured in vitro), i.e., creatine (Cre), glutamate (Glu), myo-inositol (Myo), phosphocholine (PCh), N-acetyl-aspartate (NAA), alanine (Ala), lactate (Lac), lipid at 1.3ppm (Lip1), and lipid at 0.9ppm (Lip2). These components are significant biomarkers for normal brain tissue, tumor tissue, and necrosis tissue in pathology (Howe et al., 2003). To choose proper parameters for amplitude, damping, phase and frequency for the simulated signals, we rely on a parameter extraction procedure (Poullet et al., 2006).

In order to emulate the variability within an MRSI grid, 4dB white Gaussian noise, which is in agreement with our *in vivo* signals, is added to the spectrum of each voxel.

The generated time domain signals, each having 2048 points, are Fourier transformed into the frequency domain, then truncated to the frequency range of interest, 0.25 – 4.2 ppm.

The simulated tissue-specific spectra with noise are shown in the first row of Figure 2 (in blue) and are compared with spectra from a clinical *in vivo* case as shown in the second row of Figure 2. The simulated pure spectra are in red.

3.3 Tissue type differentiation using NMF algorithms

Several NMF algorithms listed in section 2 are applied to the simulated grid described in section 3.1; see Table 1. The number of brain tissue types is set to be 3, indicating normal tissue, tumor tissue and necrotic tissue. The recovered constituent spectra

Table 1: Simulated tissue-specific spatial distribution. C denotes control tissue type, i.e., normal tissue. T denotes tumor tissue. N denotes necrotic tissue.

C	C	C	C	C	C	C	0.8C +0.2T	0.3C +0.7T	T	T	0.6T +0.4N	T
C	C	C	C	C	C	C	0.8C +0.2T	0.3C +0.7T	T	T	0.3T +0.7N	0.5T +0.5N
C	C	C	C	C	C	C	0.8C +0.2T	0.3C +0.7T	T	0.3T +0.7N	0.2T +0.8N	0.3T +0.7N
C	C	C	C	C	C	C	0.8C +0.2T	0.3C +0.7T	T	0.1T +0.9N	N	0.3T +0.7N
C	C	C	C	C	C	C	0.8C +0.2T	0.3C +0.7T	T	0.1T +0.9N	N	0.4T +0.6N
C	C	C	C	C	C	C	0.8C +0.2T	0.3C +0.7T	0.5C +0.5T	T	0.5T +0.5N	0.5T +0.5N
C	C	C	C	C	C	C	C	0.8C +0.2T	0.8C +0.2T	0.5C +0.5T	0.3C +0.7T	0.5C +0.5T
C	C	C	C	C	C	C	C	C	C	0.8C +0.2T	0.8C +0.2T	0.8C +0.2T
C	C	C	C	C	C	C	C	C	C	C	C	C
C	C	C	C	C	C	C	C	C	C	C	C	C
C	C	C	C	C	C	C	C	C	C	C	C	C

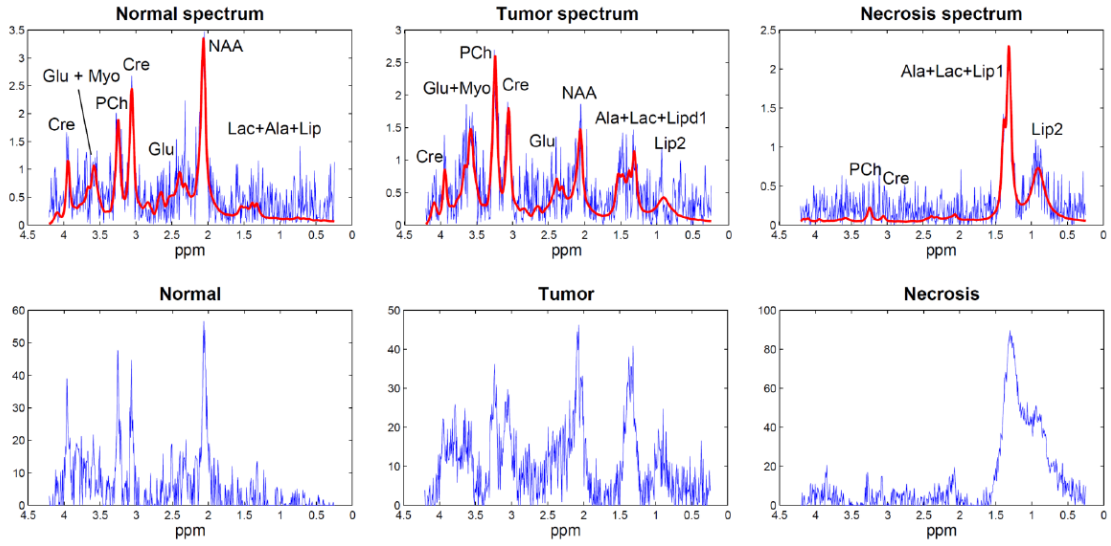


Figure 2: Spectra with SNR of 4dB from different voxels. The first row shows simulated spectra from normal tissue, tumor tissue and necrotic tissue, respectively. Simulated noiseless spectra are shown with thick red lines. For comparison, the last row contains *in vivo* spectra from the three different tissue types.

and their corresponding spatial distributions show the variability of tissue type differentiation using each of the described NMF algorithms; see Figure 3. After scaling and normalization, we notice that similar spectra with important peaks, which are biomarkers for discrimination of different tissue types (NAA, Cho, Lac/Lip), are obtained for each tissue type with all methods. The corresponding abundance maps clearly show the location of each tissue type.

3.4 Validation of spectral separation and abundance estimates

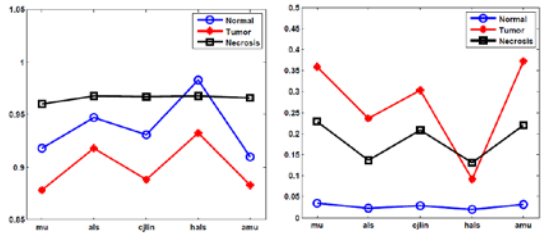
In order to evaluate the accuracy of the algorithms listed in section 2, averaged results from 500 runs (results with convergence problems were excluded, i.e. 8 out of 500 runs for **mu**, 9 out of 500 runs for **als**) for each algorithm were calculated, with different starting values. For every run, all the methods take the same initial value. Specifically, correlation coefficients R between constituent spectra estimated by NMF and simulated spectra are computed. The closer R to 1, the better the similarity between spectra generated using NMF and the simulated spectra, thus the better the performance. Furthermore, we compute the error rate of the corresponding spatial distribution for each tissue type:

$$Error\,Rate = \frac{\sum (h_e - h_s)^2}{\sum h_s^{\,2}} \cdot 100\% \qquad (9)$$

where h_e is the estimated abundance map from NMF and h_s is the original distribution (see Table 1) When the value of the error is lower, the accuracy of the estimated spatial distribution is higher.

Algorithms were adjusted to make sure they all detect convergence according to the same stopping criterion, namely the condition that $\| W^{(t+1)} - W^{(t)} \|$ or $\| H^{(t+1)} - H^{(t)} \|$ (i.e., the difference of recovered sources or the recovered abundance maps in subsequent iterations) drops below a certain tolerance level, set to 10^{-4} for all the methods.

Results are shown in Figure 4. Overall, **hals** gives the best result for all tissue types, especially the error rate calculated by **hals** for tumor is significantly lower than for other methods. Results of **ahals** were also investigated but not shown here since they are identical to **hals**.



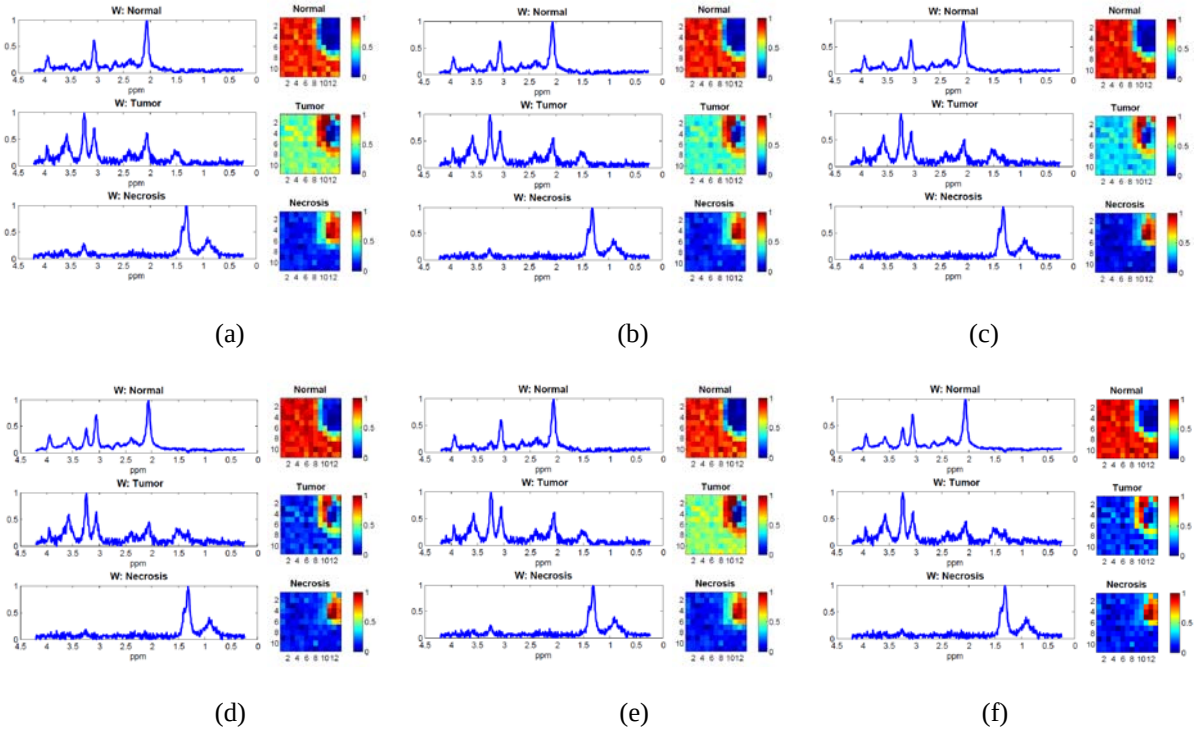
(a) (b)

Figure 4: Accuracy evaluation. (a) correlation coefficient; (b) error rate.

5 DISCUSSION & CONCLUSION

In this simulation study, we aimed at comparing the performance of several NMF algorithms on spectra with a high noise level. Spectral distortions due to, e.g., magnetic field inhomogeneity and the chemical shift displacement effect may lead to more signal variability and to the violation of the model in Eq.1. We chose not to include such non-linear factors of variability in the simulations because those would obscure the reasons for differences between methods. Nevertheless, in vivo signals need to be reprocessed and significantly distorted signals need to be excluded before spectral separation using NMF.

Among the tested NMF implementations, Lee and Seung's algorithm **mu** (Lee et al., 2001) was the most commonly used one in the past. Comparisons between various NMF algorithms have already been presented in the literature (Kim et al., 2007). But previous comparisons between algorithms were mostly focused on evaluating computational efficiency and divergence problems (Kim et al., 2007; Cichocki et al., 2009), which are indicated by the cost function $|| X - WH ||_F^2$. However, the accuracy of estimated tissue type profiles and the corresponding spatial location is much more important in the clinical diagnosis than computational speed since the computing time of all the methods is affordable for the dimensions of the considered MRSI grids. Instead of evaluating the results only visually, we follow (Croitor Sava et al., 2010) who calculated correlation coefficients between the obtained tissue sources and reference tissue models. Our error rate is calculated between the estimated spatial information and the simulated spatial information. In this way, the accuracy of the estimated spatial distribution of each tissue type can be evaluated.



(a) (b) (c)

(d) (e) (f)

Figure 3: Simulation results of normalized recovered spectra (left column) and their corresponding spatial distribution (right column) averaged over successful runs among 500 runs with different initializations using several NMF algorithms: (a) mu; (b) cjlin; (c) als; (d) hals; (e) amu; (f) ahals. The color bars show scales for the distribution of concentration.

Overall, our results show that **(a)hals** gives the best results in the simulation study, which confirms the argumentation in (Gillis, 2011) that **(a)hals** has remarkable performances. Especially the error for tumor tissue shows a significant decrease compared to all other methods. It demonstrates that the very recent NMF algorithms **hals** and **ahals** can be suitable for solving brain tissue type differentiation problems using MRSI signals. In another study, we further validate the feasibility of utilizing NMF algorithms for brain tumor tissue differentiation using *in vivo* MRSI signals.

ACKNOWLEDGEMENTS

This research was supported by Research Council KUL: GOA MaNet, CoE EF/05/006 Optimization in Engineering (OPTEC), PFV/10/002 (OPTEC), IDO 08/013 Autism, several PhD/postdoc & fellow grants; Flemish Government: FWO: PhD/postdoc grants, projects: FWO G.0302.07 (SVM), G.0341.07 (Data fusion), G.0427.10N (Integrated EEG-fMRI), G.0108.11 (Compressed Sensing) research communities (ICCoS, ANMMM); IWT: TBM070713-Accelero, TBM070706-IOTA3, TBM080658-MRI (EEG-fMRI), PhD Grants; IBBT Belgian Federal Science Policy Office: IUAP P6/04 (DYSCO, `Dynamical systems, control and optimization', 2007-2011); ESA AO-PGPF-01, PRODEX (CardioControl) C4000103224; EU: RECAP 209G within INTERREG IVB NWE programme, EU HIP Trial FP7-HEALTH/ 2007-2013 (n° 260777) (Neuromath (COST-BM0601): BIR&D Smart Care. Li thank the China Scholarship Council.

REFERENCES

Berry M, Browne M, Langville A, Pauca V, and Plemmons R, 2007. Algorithms and applications for approximate non-negative matrix factorization. *Comput Stat Data Anal*,52:155-173.

Brown T, Kincaid B, Ugurbil K, 1982. NMR chemical shift imaging in three dimensions. *PNAS*, 79(11): 3523-3526.

Cichocki A, Zdunek R, Amari S, 2007. Hierarchical ALS algorithms for nonnegative matrix and 3D tensor factorization. *Lect Notes Comput Sci*, 4666:169-176.

Cichocki A, Phan AH, 2009. Fast local algorithms for large scale Nonegative Matrix and Tensor Factorizations. IEICE Trans Fund Electron *Comm Comput Sci*, 3:708-721.

Croitor Sava AR, Sima DM, Martinez-Bisbal MC, Celda B, Van Huffel S, 2010. Non-negative Blind Source Separation Techniques for Tumor Tissue Typing Using HR-MAS signals. *In Proceedings of the 32nd Annual International Conference of the IEEE EMBS, Buenos Aires, Argentina*.

Gillis N, 2011. *Nonnegative matrix factorization complexity, algorithms and applications*. PhD Thesis, Louvan-La-Neuve, Belgium.

Gonzalez EF, Zhang Y, 2005. Accelerating the Lee-Seung algorithm for non-negative matrix factorization. *Tech Report*, Rice University.

Grippo L, Sciandrone M, 2000. On the convergence of the block nonlinear Gauss-Seidel method under convex constraints. *Oper Res Letter*, 26:127-136.

Howe FA, Barton SJ, Cudlip SA, Stubbs M, Saunders DE, Murphy JR, Opstad KS, Doyle VL, McLean MA, Bell BA, Griffiths JR, 2003. Metabolic profiles of human brain tumours using quantitative in vivo 1H magnetic resonance spectroscopy. *Magn Res Med*,49:223-232.

Jolliffe IT. Principal Component Analysis. Second edition, New York: Springer-Verlag 2002. 487 p.

Kim D, Sra S., Dhillon IS, 2007. Fast Newton-type Methods for the Least Squares Nonnegative Batrix Approximation Problem. *In Proceedings of the 2007 SIAM International Conference on Data Mining (ICDM), Pisa, Italy*.

Ladroue C, Howe FA, Griffiths JR, Tate AR, 2003. Independent component analysis for automated decomposition of in vivo magnetic resonance spectra. *Magn Reson Med*, 50:697-703.

Lee DD, Seung HS, 1999. Learning the parts of objects by non-negative matrix factorization. *Nature*, 401:788-791.

Lee DD, Seung HS, 2001. Algorithms for Non-negative Matrix Factorization, *Advances in Neural Information Processing Systems*, 13:556-562.

Lin CJ, 2007. Projected Gradient Methods for Nonnegative Matix Factorization, *Neural Comput*, 19:2756-2779.

Poullet JB, Sima DM, Simonetti AW, De Neuter B, Vanhamme L, Lemmerling P, Van Huffel S, 2006. An automated quantitation of short echo time MRS spectra in an open source software environment: AQSES. *NMR Biomed*, 20: 493-504.

Stoyanova R, Brown TR, 2001. NMR spectral quantitation by principal component analysis. *NMR Biomed*, 14:260-264.

Su Y, Thakur SB., Karimi S, Du S, Sajda P, Huang W, Parra LC, 2008. Spectrum separation resolves partial-volume effect of MRSI as demonstrated on brain tumor scans. *NMR Biomed*, 21:1030-1042.

Szabo de Edelenyi F, Simonetti AW, Postma G, Huo R, Buydens LMC, 2005. Application of independent component analysis to 1H MR spectroscopic imaging exams of brain tumours. *Anal. Chim. Acta*, 544:36-46.